Ionics
https://doi.org/10.1007/s11581-017-2386-1

ORIGINAL PAPER

Nanowires of spinel cathode material for improved lithium-ion storage

Wangwang Xu[1] · Ying Wang[1]

Received: 11 September 2017 / Revised: 28 November 2017 / Accepted: 2 December 2017

Abstract

Li-excess layered materials, such as $Li[Li_{0.2}Mn_{0.54}Ni_{0.13}Co_{0.13}]O_2$ (LMNCO) et al. are promising cathode materials that can be used in batteries for hybrid electric vehicles (HEV)/electric vehicles (EV), due to their excellent lithium-storage capability and very high energy density. Dramatic capacity loss during electrochemical cycling seriously hinders their practical implementation. It is found that the LMNCO layered cathode material suffers from structural instability and irreversible layered-to-spinel phase transition during lithiation/delithiation, leading to dramatic loss of capacity and deteriorated electrochemical kinetics. To overcome this challenge, we synthesize spinel-structured LHMNCO TBA nanowires using an electrospinning method followed by facile ion-exchange promoted phase transition. After 100 electrochemical cycles at the specific current 0.5 C, spinel-structured LHMNCO TBA still retains a capacity of about 200 mAh/g, corresponding to a capacity retention ratio of 90.5%, much higher than that of layered LMNCO nanowires, which only maintains a specific capacity of 137 mAh/g with only 48.9% capacity retention.

Keywords Li-excess materials · Nanowires · Cathode · Phase transformation · Spinel crystal structure

Introduction

The fast increasing demand for high-power and high-efficient energy system has stimulated continuous research in energy storage devices [1]. Since invented in 1991, lithium-ion batteries (LIBs) have attracted tremendous attention and gradually dominated the energy supply market for portable electronic devices, owing to their advantages of long cycle life, high efficiency in energy delivering, environmental friendly as well as light weight [2, 3]. Up to date, practical applications of LIBs are still hindered by the limited capacity, energy densities, and cycle stability from expanding to broader applications, such as stationary energy storage, cost-effective HEVs and EVs [4, 5]. Tremendous progress has been achieved on obtaining various alternative anode materials with large capacity, such as nanoscale silicon/tin-based composites, [6, 7] nitrogen-doped carbon [8], and transition metal oxides/sulfides [9], etc. These materials have demonstrated larger specific capacities as well as superior rate capability than current commercial graphite anodes [10]. However, cathode materials usually supply much lower specific capacity and exhibit worse rate capability than those of anodes, and are more crucial to the capacity of the full battery. Therefore, it is significant to develop novel cathode materials with high performance to meet the increasing demands.

Recently, various materials have been exploited as novel cathodes for LIBs, such as polyanionic compounds ($Li_3V_2(PO_4)_3$, $LiFePO_4$) [11, 12], transition metal oxides (V_2O_5, MoO_3) [13, 14], and layered $LiMO_2$ (M = Co, Ni, Mn) composite materials [15]. Among them, the emerging Li-rich manganese layered oxides have attracted more and more interest since they have a very large reversible theoretical capacity of about 250 mAh/g accompanying with high operating voltage for 3.5 V vs. Li/Li^+ [16–18]. Moreover, the Li-rich manganese layered oxides also exhibits remarkable thermal and electrochemical stabilities [19]. Therefore, Li-excess layered oxides are expected to satisfy the requirements of future energy storage systems because of their high power density and energy density [20, 21]. One of the typical examples is Li-excess ternary manganese-nickel-cobalt oxide, which is composed of

---

Electronic supplementary material The online version of this article (https://doi.org/10.1007/s11581-017-2386-1) contains supplementary material, which is available to authorized users.

✉ Ying Wang
ywang@lsu.edu

[1] Department of Mechanical & Industrial Engineering, Louisiana State University, Baton Rouge, LA 70803, USA

excess lithium ions and three common transition metals with the general formula of $Li[Li_xM]O_2$ (M = Mn, Ni, and Co). For example, $Li[Li_{0.2}Mn_{0.54}Ni_{0.13}Co_{0.13}]O_2$ (marked as LMNCO) has a very high theoretical specific capacity of 321 mAh/g with a broad voltage range from 2.0 to 4.8 V, which is much larger than that of current commercial cathode material $LiCoO_2$ (140 mAh/g). For a long time, LMNCO suffers from the problems of low rate capability and poor capacity retention resulted from serious irreversible oxygen loss during cycling. Over the years, much endeavor has been devoted to boosting the electrochemical performance of layered oxide systems. Currently, the most widely used strategies are nanostructure design and crystalline structure modification. For instance, as reported by Sun et al., at the specific current of 6 C for 50 cycles, $Li[_{Li1/3\text{-}2x/3}Ni_xMn_{2/3\text{-}x/3}]O_2$ nanoplates can still maintain a specific capacity of 197 mAh/g, which is far larger than that of the LNMO particles (40 mAh/g) [22]. This work proves that nanostructure design can improve the rate capability of active material due to the short ion transportation of nanostructure as well as large specific surface area. Among various nanostructures, 1D nanowire is a very attractive morphology because its nonwoven fabric morphology constructed by the crystalline nanowires can restrain the aggregation and growth of grains at high sintering temperature. The potential barrier among the nanosize grains can be overcome to reduce the electronic resistance among the nanosize grains [23]. In addition, the stress of the Jahn-Teller distortion of spinel-structured LHMNCO TBA nanowires can also be effectively released due to the facile strain relaxation [24–26].

Nanostructure design alone is not enough to overcome the low capacity retention of LMNCO, which is resulted from continual and inevitable layer to spinel phase transformation during cycling. As reported in literature, there are two components in the LMNCO, the layered lithium-inactive Li_2MnO_3 and the layered lithium-active $LiMn_{1/3}Ni_{1/3}Co_{1/3}O_2$ with a molar ratio of 1:1 [27]. During the delithiation and lithiation process, layered Li_2MnO_3 gradually converts into numerous spinel grains, which are integrated in an amorphous matrix. Simultaneously, the structure of $LiMn_{1/3}Ni_{1/3}Co_{1/3}O_2$ rearranges by the migration of transition metal ions into the layers of lithium-ion [28, 29]. The formed spinel grains may contribute to the rate capability, because of their facile lithium-ion diffusivity and higher electronic conductivity. However, the formation process of spinel structure during cycling smashes the layered lattice and generates strains, resulting structural instability, low coulombic efficiency, and poor electrochemical reversibility. Various methods have been reported to avoid the irreversible capacity loss and to further improve the cycling life of LMNCO, such as doping, [30] surface modification [31], and phase transformation [20]. Recently, an ion-exchange promoted phase transition for LMNCO materials has been reported by Zhao et al. [20]. At the specific current of 1 C for 100 cycles, the transformed $Li_4Mn_5O_{12}$-type spinel cathode material can provide a specific capacity as large as 197.5 mAh/g with excellent reversibility, demonstrating remarkably improved rate capability and prolonged cycling life. This result proves that phase transition is an effective way to enhance performance of ternary cathode materials.

Herein, we design and synthesize Li-excess spinel cathode nanowires, to combine the merits of excellent structural stability of $Li_4Mn_5O_{12}$ and facile stress release of the Jahn-Teller distortion during cycling owing to its 1D nanostructure [32]. The overall synthesis strategy is schematically illustrated in Fig. 1. In step I, nanowires are prepared by an electrospinning process of the precursor solution. In step II, layered $Li[Li_{0.2}Mn_{0.54}Ni_{0.13}Co_{0.13}]O_2$ nanowires are synthesized via two steps of heat treatment. In step III, the $Li_4Mn_5O_{12}$-type spinel nanowires are obtained by ion-exchange promoted phase transition. There are several unique properties of LMNCO spinel nanowires as the cathode material for LIBs: (1) owing to the very large specific surface area, 1D LMNCO spinel nanowires, can provide shorter diffusion length and more active reaction sites. (2) The facile strain relaxation in the nanowires allows them to increase in diameter without breaking, leading to excellent mechanical integration during lithiation/delithiation. Moreover, the 1D LMNCO spinel nanowires, which are assembled by small nanoparticles can effectively prevent the aggregation of nanoparticles. (3) The LMNCO spinel phase can realize better rate capability and cycling stability. In addition, by using time-resolved in situ X-ray diffraction (XRD) characterizations, we further investigate the crystalline stability of LMNCO spinel nanowires during long electrochemical cycling. As far as we are concerned, this work is the first effort to achieve nanowires of Li-excess spinel cathode material. In this structure, the merits of stable LMNCO spinel phase can be effectively combined in 1D nanowires with high specific surface area, yielding a cathode material with improved rate capability and long cycling life. Therefore, it is anticipated that the as-prepared Li-excess spinel cathode nanowires would display excellent rate performance and prolonged cycling life.

Experimental section

All the raw materials are purchased from Alfa Aesar

Synthesis of layered LMNCO nanowires The 1D LMNCO nanowires were synthesized by the combination of electrospinning and a subsequent sintering treatment. For a typical synthesis, polyvinyl pyrrolidone (PVP, MW =

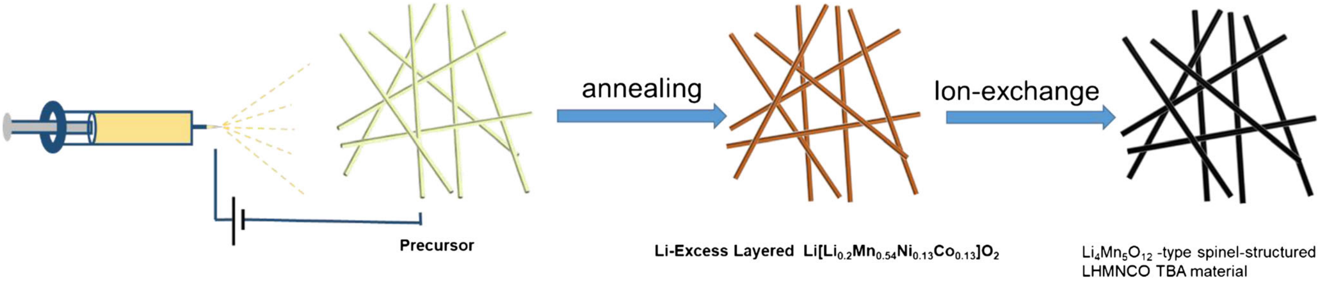

Fig. 1 Schematic illustrations showing the synthesis process of preparation of spinel LHMNCO TBA nanowires

36,000, 2 g), $Co(CH_3COO)_2{\cdot}4H_2O$ (0.0324 g), $Ni(CH_3COO)_2{\cdot}4H_2O$ (0.0323 g), $Mn(CH_3COO)_2{\cdot}4H_2O$ (0.1323 g), and $LiCH_3COO{\cdot}2H_2O$ (0.079 g) were dissolved in 15 mL dimethyl-formamide with stirring for 6 h at room temperature. A brown solution with certain viscosity was obtained. Then, electrospinning was conducted with a constant flow rate of 0.3 mL/h. The spinning voltage was set at 17 kV, and the distance between the spinneret and collector was 18 cm. Finally, the as-prepared nanofibers were initially annealed at 300 °C for 2 h and then treated at 750 °C for 8 h in air with the heating rate of 2 °C/min.

Ion exchanges in layered LMNCO nanowires The H^+-Li^+ cation exchange of $Li[Li_{0.2}Mn_{0.54}Ni_{0.13}Co_{0.13}]O_2$ nanowires was conducted in aqueous HCl solution. Two hundred milligrams $Li[Li_{0.2}Mn_{0.54}Ni_{0.13}Co_{0.13}]O_2$ nanowires were dispersed in 150 mL 2 M HCl solution, followed with stirring at room temperature for 10 days. Afterwards, the obtained brown powder was collected by centrifugation. The TBA^+-H^+ cation exchange was performed by employing aqueous tetrabutylammonium hydroxide (TBAOH) solution. The obtained brown powder was dispersed into a 30-mL TBAOH solution, followed with vigorous stirring for 1 h. The resulting products were collected via centrifugation, rinsed with deionized water and ethanol for several times and dried at 80 °C overnight. After that, the ion-exchanged derivative was dispersed in a crucible, heated to 500 °C with a heating rate of 1 °C/min, and kept at that temperature for 3 h in the furnace.

Characterization Crystallographic features of the synthesized products were characterized by Rigaku MiniFlex X-ray diffraction (XRD) measurement with Cu X-ray source. The diffraction data were collected in the 2θ range of 10–80° at a scan rate of $1°\ \text{min}^{-1}$. Field emission scanning electron microscope (FESEM) images and energy dispersive spectroscopic (EDS) were collected by using a FEI Quanta 3D FEG. Transmission electron microscopic (TEM) images and high-resolution transmission electron microscopy (HRTEM) were taken using a JEOL HRTEM (JEM-1400 electron microscope) with an acceleration voltage of 120 kV. The in situ XRD patterns of the samples were obtained with a D8 DISCOVER X-ray diffractometer, using Cu Kα radiation ($\lambda = 1.5418$ Å). For in situ XRD measurement, the as-prepared electrode was placed right behind an X-ray-transparent beryllium window which also acts as a current collector. The in situ XRD signals were collected using the planar detector in a still mode during 40 electrochemical cycles with voltage range of 2–4.8 V (versus Li^+/Li).

Electrochemical measurements The cathode was composed of the as-prepared LMNCO based material (layered LMNCO nanowires, $Li_4Mn_5O_{12}$-type spinel nanowires), carbon black and polytetrafluoroethylene (PTFE) mixture with a weight ratio of 7:2:1. The cathode was assembled into CR2032 coin cells in glove-box filled with pure argon. The counter electrode was the lithium foil and the electrolyte was 1 M solution of LiPF6 in ethylene carbonate (EC) and dimethyl carbonate (DMC) and diethylcarbonate (DEC) at a volumetric ratio of 1:1:1. Celgard-2320 membrane was used as separator. The batteries were aged for 24 h to ensure full filtration of the electrolyte into the electrodes. Galvanostatic charge-discharge measurements were conducted in a voltage range of 2–4.8 V (versus Li^+/Li) with an eight-channel battery analyzer (MTI Corporation). Cyclic voltammetry (CV) and AC-impedance spectra were performed by using an electrochemical work station (CHI 6504C).

Result and discussion

The schematic illustration of the chemical reaction during synthesis procedure is displayed in Fig. 1. In the first step, LMNCO nanowires are protonated in aqueous HCl solution, in which Li^+ ions are partially substituted by H^+ ions. This protonation process is the prerequisite for the following ion-exchange step, which induces a detectable spinel phase transformation in a predominant layered crystal. The second ion exchange was performed in TBAOH solution, in which H^+ ions in the layered intermediate LMNCO nanowires are further replaced by larger (tetrabutylammonium ion) TBA^+ cations. And the intercalation of TBA^+ into the interlayer space leads to the expanded interlayer space. Such expanded layered structure contributes to the favorable generation of lithium-ion vacancies and subsequent displacement of transition metal cations after the removal of TBA^+ via calcinations in air, and thus leads to a complete layered-to-spinel phase transition. The larger TBA^+ cations further induce the transformation of the layered phase into the spinel phase during sintering at 500 °C in air.

To investigate the phase transformation from layered Li-excess LMNCO to spinel-structured LHMNCO TBA nanowires, the crystal structure of these two nanowires is determined by XRD. Figure 2a, b display ex situ XRD patterns of layered Li-excess LMNCO as well as ion exchange promoted spinel-structured LHMNCO TBA nanowires. From Fig. 2a, pristine LMNCO shows typical XRD peaks, exhibiting the intergrowth of monoclinic Li_2MnO_3 with C2/m symmetry and rhombohedral $LiMn_{1/3}Ni_{1/3}Co_{1/3}O_2$ with R-3 m symmetry in an ordered layered crystal structure. The coupled peaks at $2\theta = 64°–66°$ are the characteristic of $LiMn_{1/3}Ni_{1/3}Co_{1/3}O_2$, which is the predominant layered crystal component. The integration of rhombohedral $LiMn_{1/3}Ni_{1/3}Co_{1/3}O_2$ and monoclinic Li_2MnO_3 are deduced from the following three peaks at $2\theta = 18.7°$, 36.9°, and 44.5°. These three peaks merge the diffraction effects from $(001)_M/(003)_R$, $(200)_M/(101)_R$, and $(202)_M/(104)_R$, respectively. Figure 2b shows the XRD pattern of the spinel-structured LHMNCO TBA nanowires. In comparison with the pattern of layered Li-excess LMNCO, it is found that the separated couple peaks at 64°–65° are merge into one (440) peak, indicating a complete layer to spinel phase conversion. The as-prepared product can be indexed as a spinel $Li_4Mn_5O_{12}$ phase with an Fd-3 m space group instead of usual $LiMn_2O_4$-type spinel due to different characteristic XRD peak positions at higher diffraction angles [20].

SEM and EDS are used to characterize the morphology and elementary composition of the samples, as displayed in Fig. 3. Figure 3a–d show the SEM images of electrospun nanofibers before sintering, nanofibers after sintering at 300 °C, layered Li-excess LMNCO nanowires, and spinel-structured LHMNCO TBA nanowires, respectively. As observed clearly in Fig. 3a, the electrospun nanofibers are smooth and uniform before annealing. The diameter of electrospun nanofibers is about 150 nm. Notably, after sintering at 300 °C for 2 h, electrospun nanofibers shrink due to the decomposition of PVP (Fig. 3b). After sintering at 750 °C for 8 h, the as-prepared layered Li-excess LMNCO inherits the nanowire-in-network morphology. As displayed clearly in the inserted high-magnification SEM image in Fig. 3c, the layered Li-excess LMNCO nanowires are composed of small interconnected nanoparticles. After ion exchanges in layered LMNCO nanowires, the obtained spinel-structured LHMNCO TBA nanowires maintain the nanowire-in-network morphology (Fig. 3d). Moreover, the elemental distribution of spinel-structured LHMNCO TBA nanowires is clearly confirmed by the EDS mappings. As shown in Fig. 3e, the Mn, Ni, Co, and O signals for spinel-structured LHMNCO TBA nanowires, are overlapped uniformly across the entire sample, indicating uniform formation of the spinel-structured LHMNCO TBA nanowires. In addition, the elemental information of spinel-structured LHMNCO TBA nanowires has been added in Table S1. It is found that the elemental ratio of Ni:Co:Mn:O is 1:0.70:4.66:6.50 in the spinel-structured LHMNCO TBA nanowires. Cobalt and nickel loss can probably be attributed to dissolution during acid leaching. The H^+-Li^+ ion exchange or the formation of Li_2O may cause an internal redox reaction on the transition metal sites and dissolution of the transition metals as an oxide for the charge compensation. To further identify the nanostructure and crystallographic information of spinel-structured LHMNCO TBA nanowires, TEM and HR-TEM coupled with electron diffraction characterizations are carried out. Figure S1 presents the TEM image of spinel-structured LHMNCO TBAnanowires, confirming the nanowires are assembled with small nanoparticles with average diameter of 80 nm. Meanwhile, HRTEM images of monocrystalline layered LMNCO and spinel-structured LHMNCO TBA are shown in Fig. 4a, b, respectively. Figure 4a reveals lattice fringes with spacings of 0.47 nm, corresponding to (003) planes of the layered LMNCO. The SAED pattern (inset in Fig. 4a) is well indexed as a monocrystalline layered LMNCO phase. The HRTEM image of spinel-structured LHMNCO TBA nanowires in Fig. 4b reveals the lattice fringes with spacing of 0.28 nm, corresponding to (220) plane of spinel-structured LHMNCO TBA nanowires. The SAED pattern (inset in Fig. 4b) reveals the pure spinel phase of the phase transformed LMNCO nanowires.

In order to evaluate electrochemical performances of the as-prepared samples, coin cells of layered LMNCO nanowires and spinel-structured LHMNCO TBA nanowires are assembled to investigate in a voltage range of 2–4.8 V (versus Li^+/Li). Figure 5a summarizes cycling performances of layered LMNCO nanowires and spinel-structured LHMNCO TBA nanowires, respectively at a specific current of 0.5 C. As shown in Fig. 5a, the initial discharge specific capacity of layered LMNCO nanowires and spinel-structured LHMNCO TBA nanowires are 280 and 210 mAh/g, respectively. The higher initial capacity of layered LMNCO nanowires attributes to more lithium-storage sites in the layered phase. After 100 electrochemical cycles, spinel-structured LHMNCO TBA retains a capacity of 190 mAh/g, resulting in the capacity retention ratio of 90.5%, demonstrating the enhanced discharge capacity and outstanding cycling stability. In contrast, drastic capacity fading is observed for layered LMNCO nanowires. After 100 cycles, layered LMNCO nanowires maintain only 137 mAh/g, corresponding to a capacity retention ratio of only 48.9%. To analyze the electrochemical reactions of two samples, the charge-discharge profiles and CV curves have been tested and added in Fig. 5b, c and Fig. S2. As the CV curves shown in Fig. 5b, in the first anodic

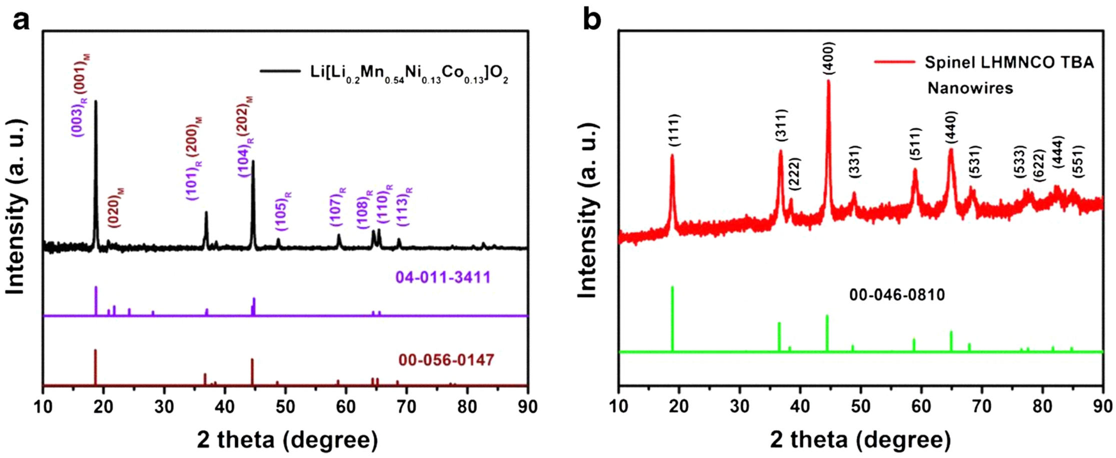

Fig. 2 XRD patterns of **a** layered Li[Li$_{0.2}$Mn$_{0.54}$Ni$_{0.13}$Co$_{0.13}$]O$_2$ nanowires and **b** spinel LHMNCO TBA nanowires

scan, two small peaks at around 2.9 V and 4.8 vs. Li/Li$^+$ are ascribed to the oxidation of Mn^{3+} and Ni^{3+} ions and the simultaneous removal of lithium ions. During the following anodic/cathodic scan, the predominant redox pair, displays an anodic peak at 3.02 V and cathodic peak at 2.48 V, which are attributed to oxidation and reduction of Mn^{3+}/Mn^{4+} in the spinel-structured LHMNCO TBA nanowires. Another two redox pairs, anodic peak at 4.00 V/cathodic peak at 4.01 V, and anodic peak at 4.70 V/cathodic peak at 4.50 V, are ascribed to oxidation/reduction of Ni^{3+}/Ni^{4+} and Co^{3+}/Co^{4+}, respectively. The galvanostatic charge-discharge curves in Fig. 5c display predominant charge and discharge voltage plateaus at 2.7 and 2.5 V, respectively, which coincide with the CV curves in Fig. 5b. Moreover, the spinel-structured LHMNCO TBA nanowires deliver a charge capacity of 270 mAh/g and charge capacity of 250 mAh/g in the 1st cycle at a current density at 0.1 C. The charge-discharge profile of the layered LMNCO nanowires in Fig. S2 shows smooth sloping voltage curves, which are consistent with the corresponding CV peaks in Fig. S2a. After initial charging process, layered LMNCO nanowires reveal predominant discharge voltage plateaus at 3.2–3.6 V and can deliver a discharge capacity of 260 mAh/g in the 1st cycle at a current density at 0.1 C. The rate performances of these two samples are summarized in Fig. 5d. The Spinel-structured LHMNCO TBA nanowires deliver a discharge capacity of 270, 246, 230, 195, and 162 mAh/g at a specific current of 0.1, 0.2, 0.5, 1, and 2 C, respectively. When the specific current goes back

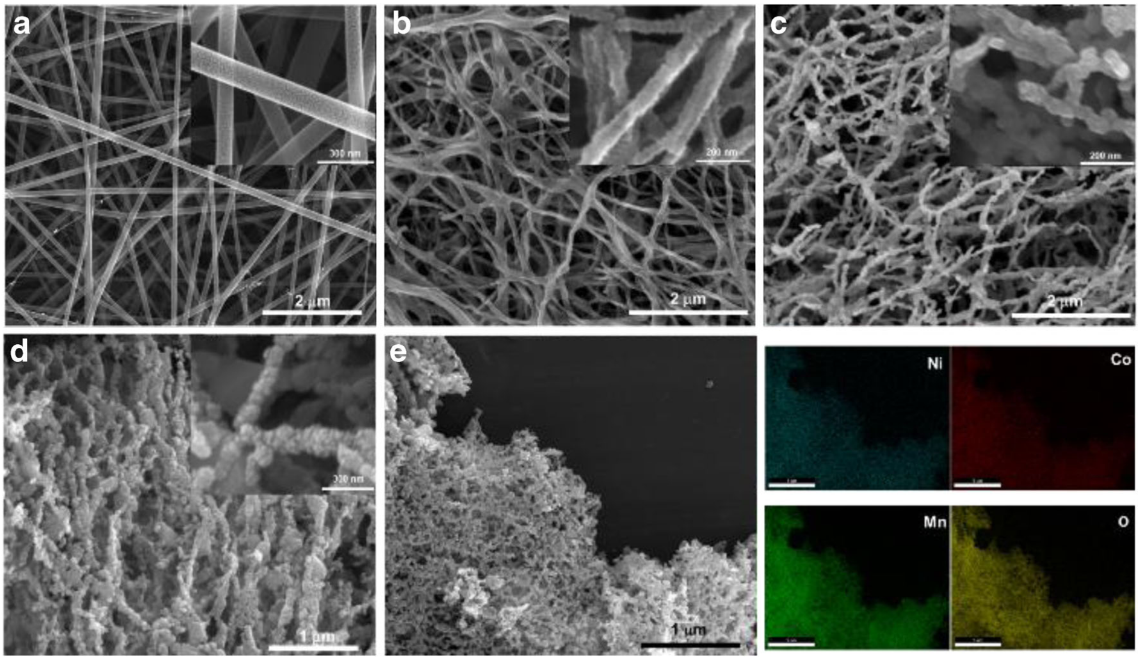

Fig. 3 SEM images of **a** as-electro-spun nanofibers, **b** nanofibers after sintered at 300 °C for 2 h, **c** layered LMNCO nanowires, **d** spinel LHMNCO TBA nanowires, and **e** EDS mapping of spinel LHMNCO TBA nanowires

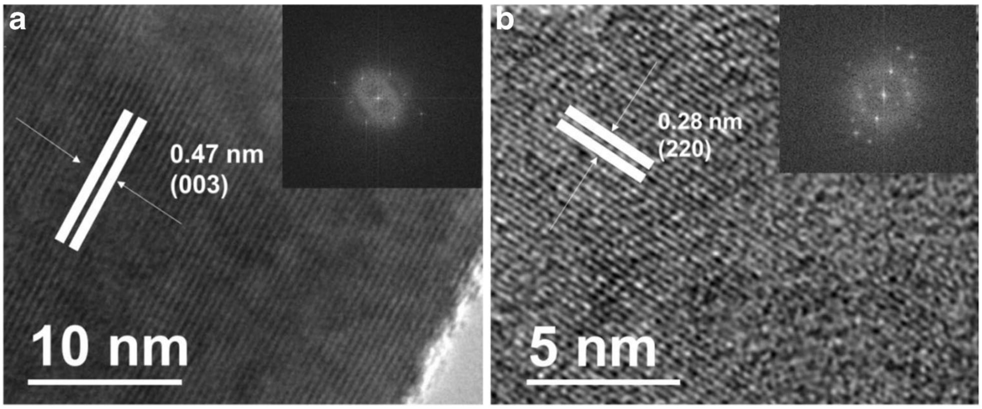

Fig. 4 The HRTEM image and SAED patterns (inset) of **a** layered LMNCO nanowires and **b** spinel LHMNCO TBA nanowires

from 2 to 0.5 C, the discharge capacity of spinel-structured LHMNCO TBA nanowires is recovered to 228 mAh/g, showing better rate capability than layered LMNCO nanowires.

To investigate the change of electrochemical kinetics in the layered LMNCO nanowires during cycling, EIS technology is employed. In the Nyquist plots, R_Ω represents the Ohmic resistance of the battery cell, including electrodes, electrolyte, and other cell components. R_{ct} represents the charge transfer resistance. CPE and Z_w are the double layer capacitance and the Warburg impedance, respectively. The Nyquist plots of all the three electrodes are composed of a depressed semicircle in the medium-frequency region followed by a slanted line in the low-frequency region. As shown in Fig. 6a, the layered LMNCO nanowires show the resistance of 150 Ω at an initial cycle and 200 Ω at the 120th cycle. The increase of the Ohmic resistance indicates the deteriorated kinetics of the electrochemical reactions after cycling. Moreover, the values of R_{ct} at the first, the 30th, the 60th, the 90th, and the 120th cycles also show gradually decreased tendency, indicating the increased charge transfer resistance with the increase in cycle

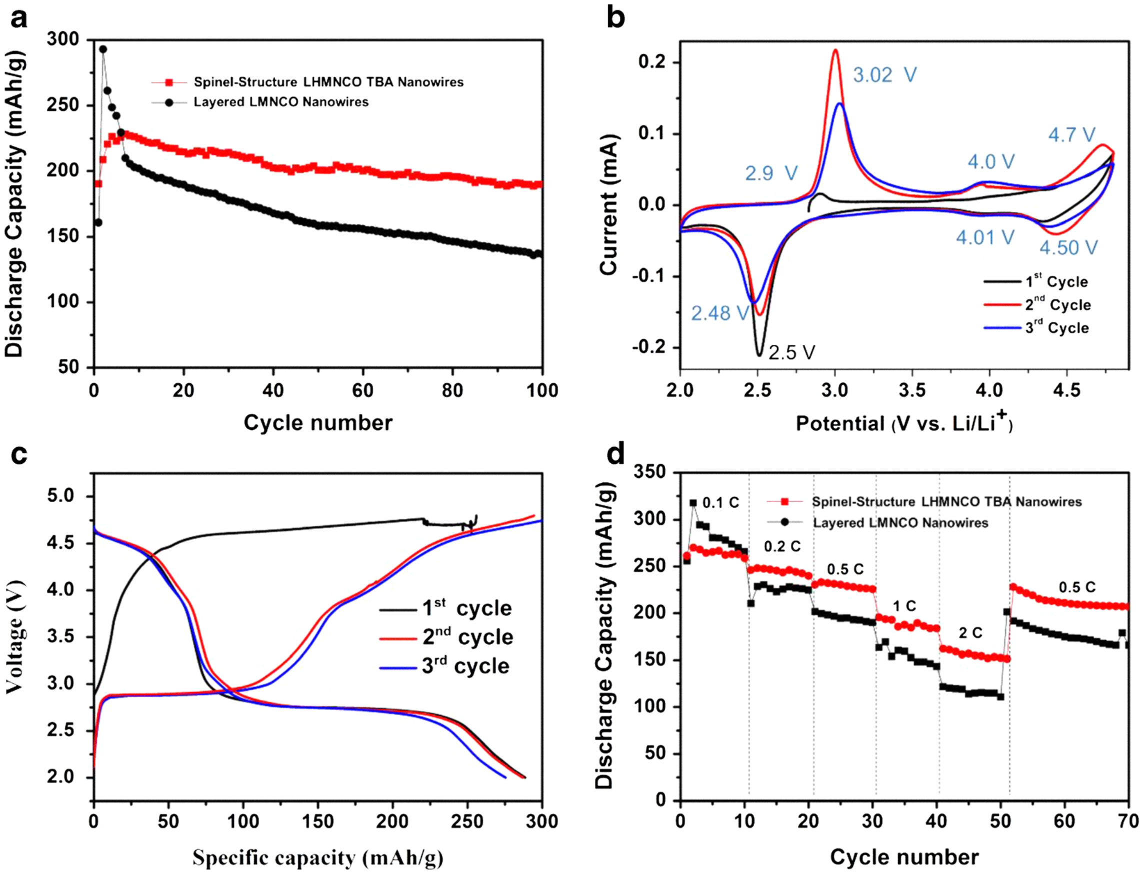

Fig. 5 **a** Cycling performance at 0.5 C, **b** CV curves at a scan rate of 0.1 mV/s, **c** charge-discharge profiles at 0.1 C, and **d** rate performance at specific currents ranged from 0.1, 0.2, 0.5, 1, 2, to 0.5 mA/g

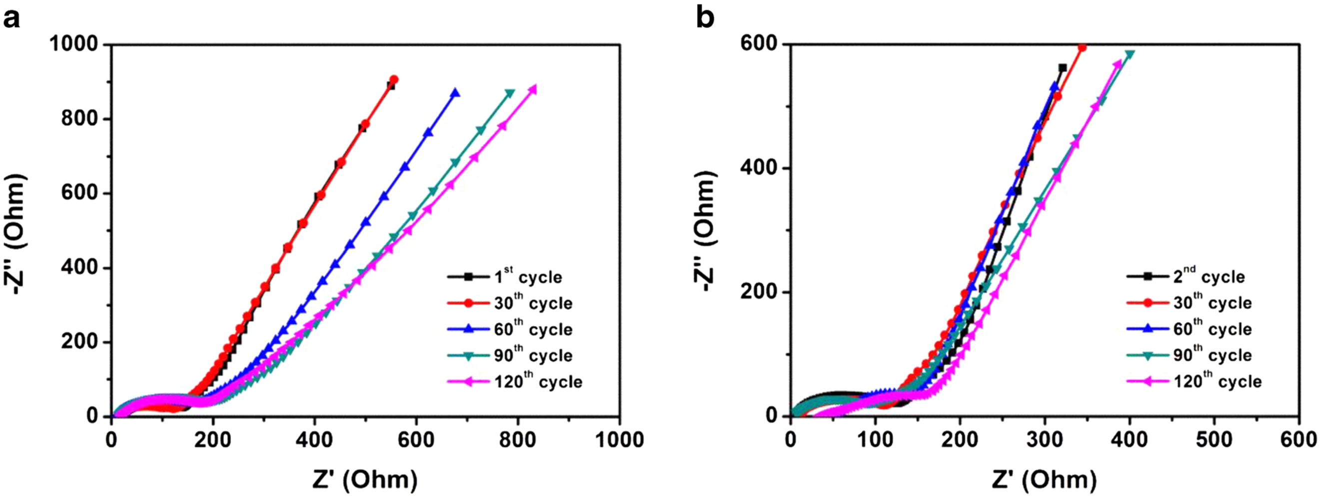

Fig. 6 EIS spectra of **a** layered LMNCO nanowires, **b** spinel LHMNCO TBA nanowires at the 1st, 30th, 60th, 90th, and 120th cycle

numbers. This is due to the phase transformation, lattice break down, and possible deteriorated interface between electrode and electrolyte that impedes the reversible intercalation/deintercalation of lithium ions. Figure S3 shows the CV profiles of the layered LMNCO nanowires of the initial cycle, the 2nd cycle, the 30th cycle, the 60th cycles, the 90th cycle, and the 120th cycle, at a scan rate of 0.1 mV/s. As shown in Fig. S3, the intensity of cathodic peak at around 4.8 V gradually decreases during cycling, indicating the continuous loss of oxygen and lithium with increased cycles. In addition, the discharge curves show obvious voltage decay. The prominent cathodic peak decreases from 3.3 V at the initial cycle to 2.4 V at the 120th cycle, revealing gradually transformation from layered structure to spinel-like structure during cycling. Figure S4 presents the charge-discharge profile of spinel-structured LHMNCO TBA nanowires at 3rd, 60th, and 120th cycle. The stable potential plateaus confirm the stable crystal structure of spinel-structured LHMNCO. Theoretically, the spinel-structured LHMNCO TBA provides more pathways for the transportation of lithium-ions, as confirmed by the EIS results in Fig. 6b. Compared to the significantly increased Ohmic resistance of the layered LMNCO nanowires after cycling, spinel-structured LHMNCO TBA shows a resistance of 130 Ω at initial cycle and 150 Ω at the 120th cycle, indicating the lower resistance and stable kinetics of the electrochemical reaction after cycling. Additionally, in comparison with the decreased tendency of R_{ct} of layered LMNCO nanowires, the slope of the plot from the spinel-structured LHMNCO TBA nanowires is high and maintained well after cycling, suggesting much lower R_{ct} value and enhanced ion diffusion kinetics of stable spinel-structured LHMNCO TBA than that of layered LMNCO nanowires. The high conductivity and improved ion diffusion of spinel-structured LHMNCO TBA nanowires are attributed to the following factors. First, the efficient 3D Li^+ diffusion channels in the spinel-structured LHMNCO TBA structure boost the Li^+ diffusion rate. In addition, nanowires can restrain the aggregation and grain growth at high temperature, leading to high surface area with short pathway for the transport of lithium-ions. Finally, the electronic resistance is decreased due to the lower barrier among the nanosize grains [33].

In addition, compared with most recently reported ternary nanostructured cathode materials (as shown in Table S1), [34–36] our work demonstrates significantly prolonged cycling life and improved discharge capacity. For example, Wang et al. reported that the $Li_{1.13}1Mn_{0.504}Ni_{0.243}Co_{0.122}O_2$ cathode materials can supply only 155.9 mAh/g after 50 cycles at a specific current of 200 mA/g, maintaining only 78.8% of the initial specific capacity (197.8 mAh/g). Moreover, Tu et al. synthesized ball-like $LiMn_{0.4}Ni_{0.4}Co_{0.2}O_2$ cathode materials. The $LiMn_{0.4}Ni_{0.4}Co_{0.2}O_2$ nanospheres can supply only 180 mAh/g at the specific current of 0.5 C, and maintain only 80% of the initial capacity after 50 cycles at 5 C. Our spinel-structured LHMNCO TBA nanowires maintain a capacity of about 200 mAh/g after 100 cycles at 0.5 C with a capacity retention ratio of 90.5%, exhibiting high capacity and excellent cycling reversibility.

In situ XRD is an emergent and effective tool for exploring the stability of battery electrode by continuously examining the diffraction peaks of the electrode material and any changes during electrochemical cycling. This technique together with HR-TEM was used to find that layered LMNCO suffers from capacity degradation and structural instability during cycling, as reported in literature [37, 38]. For instance, Daniel et al., reported that the cubic spinel planes of (440) appeared during the discharging process of the layered cathode, revealing a layer to spinel phase transformation in the lattice, which is believed to contribute to the structural instability in subsequent cycling [34]. Moreover, Hwang et al. found cracks and pores in the layered

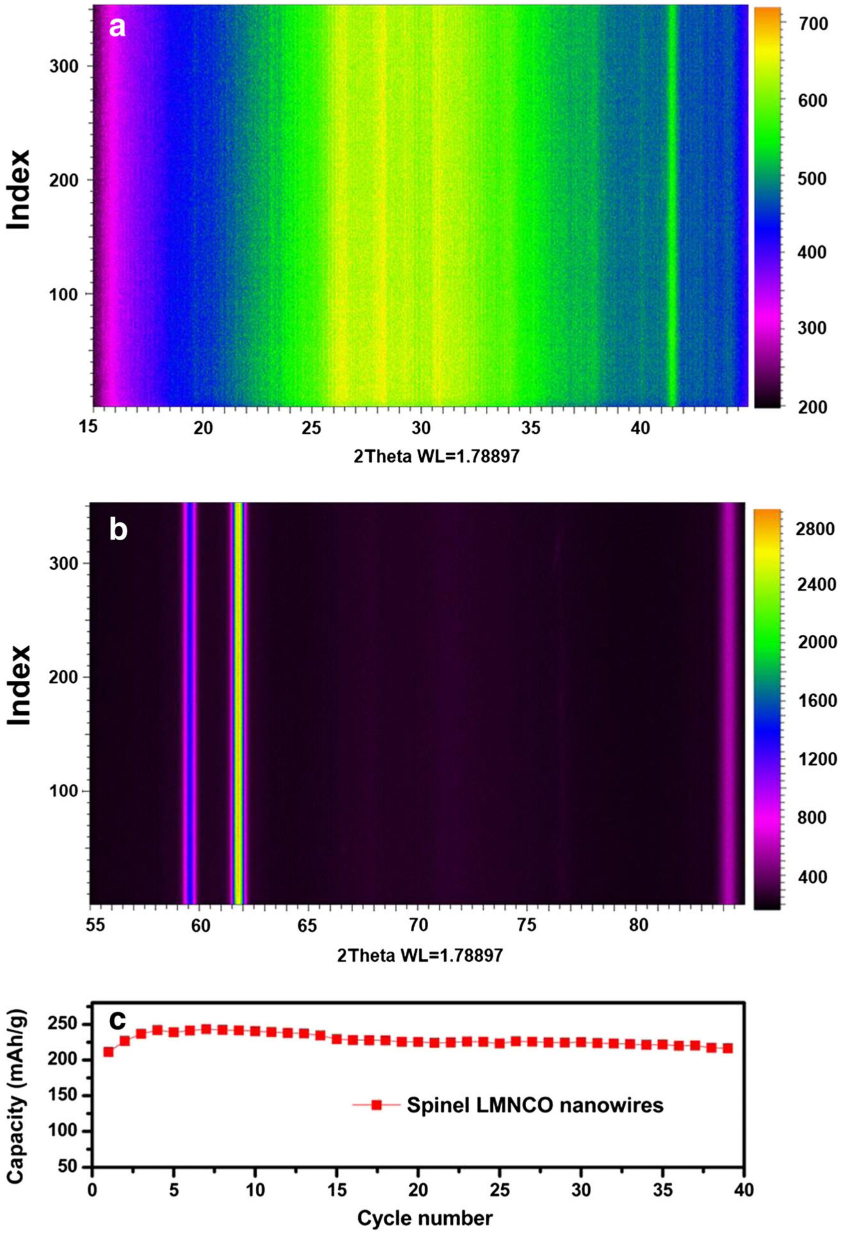

Fig. 7 In situ X-ray diffraction patterns of spinel LHMNCO TBA nanowires at a current density 0.5 C. The horizontal axis represents the selected 2θ regions from **a** 15°–45° and **b** 55°–85°. **c** The corresponding cycling curve

nanoparticles after cycling via HRTEM imaging. The layered-to-spinel phase transition produces large lattice strain, leading to the breakdown of the parent lattice [38]. In this work, we use in situ XRD to investigate the crystal structural stability of spinel-structured LHMNCO TBA nanowires, and the results are presented in Fig. 7. In Fig. 7, three peaks at $2\theta = 59.5°$, 61.7°, and 84.2° represent (511), (440), and (444) crystal planes in the cubic spinel phase. It can be clearly seen that these peaks are stable during long cycling test, indicating the robust crystal structure of spinel-structured LHMNCO TBA nanowires and demonstrating it is a superior LIB electrode material compared to the layered cathode with poor stability.

Conclusion

In summary, this work has demonstrated a simple and controllable approach for fabricating novel spinel-structured LHMNCO TBA nanowires via the electrospinning method followed by facile ion exchange promoted layered-to-spinel phase transition. For comparison purpose, the layered LMNCO nanowires are obtained as well and are found to suffer from structural instability, i.e., irreversible layered-to-spinel phase transition during lithiation/delithiation, leading to dramatic loss of capacity and deteriorated electrochemical kinetics. The newly converted spinel-structured LHMNCO TBA nanowires exhibit significant improvements in electrochemical performance as LIB cathode material, especially in capacity and cycling reversibility, as evidenced by its CV measurements and EIS plots, and further confirmed by in situ XRD examination. Such improved performance of the spinel nanowires is attributed to their 1D nanostructure and transformed spinel phase, which not only shorten the lithium diffusion length and increase the lithium-ion diffusivity, but also strengthen the structural stability. As such, the designed spinel-structured LHMNCO TBA nanowires prove to be a promising cathode material for application in advanced lithium-ion batteries with high capacity, high rate capability, and excellent stability.

Acknowledgments We acknowledge the Research Enhancement Award (REA) and Research Awards Program (RAP) sponsored by LaSPACE and the Economic Development Assistantship from LSU graduate school for financial support of this work. We thank the Shared Instrumentation Facilities (SIF) at Louisiana State University for using XPS, XRD, SEM, and TEM. We also thank Prof. L. Q. Mai, Dr. K. N. Zhao and Dr. L. Zhang of Wuhan University of Technology for the in situ XRD characterization.

References

1. Chen XX, Tang QW, He BL, Lin L, Yu LM (2014) Platinum-free binary Co-Ni alloy counter electrodes for efficient dye-sensitized solar cells. Angew Chem Int Ed 53(40):10799–10803. https://doi.org/10.1002/anie.201406982
2. Armand M, Tarascon JM (2008) Building better batteries. Nature 451(7179):652–657
3. WW X, Cui XD, Xie ZQ, Dietrich G, Wang Y (2016) Three-dimensional coral-like structure constructed of carbon-coated interconnected monocrystalline SnO_2 nanoparticles with improved lithium-storage properties. ChemElectroChem 3(7):1098–1106
4. Dunn B, Kamath H, Tarascon JM (2011) Electrical energy storage for the grid: a battery of choices. Science 334(6058):928–935. https://doi.org/10.1126/science.1212741
5. WW X, Xie ZQ, Cui XD, Zhao KN, Zhang L, Mai LQ, Wang Y (2016) Direct growth of an economic green energy storage material: a monocrystalline Jarosite-$KFe_3(SO_4)_2(OH)_6$-Nanoplates@rGO hybrid as a superior lithium-ion battery cathode. J Mater Chem A 4(10):3735–3742
6. Hui W, Chan G, Choi JW, Ryu I, Yao Y, McDowell MT, Lee SW, Jackson A, Yang Y, LB H, Cui Y (2012) Stable cycling of double-walled silicon nano-tube battery anodes through solid-electrolyte interphase control. Nat Nanotechnol 7(5):310–315
7. Li L, Zhang XX, Chen RJ, Zhao TL, Lu J, Wu F, Amine K (2014) Synthesis and electrochemical performance of cathode material $Li_{1.2}Co_{0.13}Ni_{0.13}Mn_{0.54}O_2$ from spent lithium-ion batteries. J Power Sources 249:28–34. https://doi.org/10.1016/j.jpowsour.2013.10.092
8. Xie ZQ, He ZY, Feng XH, Xu WW, Cui XD, Zhang JH, Yan C, Carreon MA, Liu Z, Wang Y (2016) Hierarchical sandwich-like structure of ultrafine N-rich porous carbon nano-spheres grown on graphene sheets as superior lithium-ion battery anodes. ACS Appl Mater Interfaces 8(16):10324–10333. https://doi.org/10.1021/acsami.6b01430
9. WW X, Xie ZQ, Cui XD, Zhao KN, Zhang L, Dietrich G, Dooley KM, Wang Y (2015) Hierarchical graphene-encapsulated hollow SnO_2@SnS_2 nanostructures with enhanced lithium storage capability. ACS Appl Mater Interfaces 7(40):22533–22541
10. Goriparti S, Miele E, Angelis FD, Fabrizio ED, Zaccaria RP, Capiglia C (2014) Review on recent progress of nanostructured anode materials for Li-ion batteries. J Power Sources 257:421–443. https://doi.org/10.1016/j.jpowsour.2013.11.103
11. Huang HS, Yin C, Kerr T, Taylor N, Nazar LF (2002) Nanostructured composites: a high capacity, fast rate $Li_3V_2(PO_4)_3$/carbon cathode for rechargeable lithium batteries. Adv Mater 14(21):1525–1528
12. Liu H, Strobridge FC, Borkiewicz OJ, Wiaderek KM, Chaman KW, Chupas PJ, Grey CP (2014) Capturing metastable structures during high-rate cycling of LiFePO4 nanoparticle electrodes. Science 344(6191):1252817. https://doi.org/10.1126/science.1252817
13. Chao D, Xia X, Liu J, Fan Z, Ng CF, Lin J, Zhang H, Shen ZX, Fan HJ (2014) A V_2O_5/conductive-polymer core/shell nanobelt Array on three-dimensional graphite foam: a high-rate, ultrastable, and free-standing cathode for lithium-ion batteries. Adv Mater 26(33):5794–5800
14. Mai LQ, Hu B, Chen W, Qi YY, Lao CS, Yang RS, Dai Y, Wang ZL (2007) Lithiated MoO_3 nanobelts with greatly improved performance for lithium batteries. Adv Mater 19(21):3712–3716. https://doi.org/10.1002/adma.200700883
15. Kong F, Longo RC, Park MS, Yoon J, Yeon DH, Park JH, Wang WH, Santosh KC, Doo SG, Cho K (2015) Ab initio study of doping effects on $LiMnO_2$ and Li_2MnO_3 cathode materials for Li-ion batteries. J Mater Chem A 3(16):8489–8500. https://doi.org/10.1039/C5TA01445J
16. Xie Y, Saubanere M, Doublet ML (2017) Requirements for reversible extra-capacity in Li-rich layered oxides for Li-ion batteries. Energy. Environ Sci 10(1):266–274
17. Xu B, Fell CR, Chi MF, Meng YS (2011) Identifying surface structural changes in layered Li-excess nickel manganese oxides in high voltage lithium ion batteries: a joint experimental and theoretical study. Energy Environ Sci 4(6):2223–2233
18. Zhao JQ, Ellis S, Xie ZQ, Wang Y (2015) Synthesis of integrated layered-spinel composite cathode materials for high-voltage lithium-ion batteries up to 5.0 V. ChemElectroChem 2(11):1821–1829. https://doi.org/10.1002/celc.201500164
19. Liu J, Liu W, Ji SM, Zhou YC, Hodgson P, Li YC (2013) Electrospun spinel $LiNi_{0.5}Mn_{1.5}O_4$ hierarchical nanofibers as 5 V cathode materials for lithium-ion batteries. ChemPlusChem 78(7):636–641. https://doi.org/10.1002/cplu.201300180
20. Zhao JQ, Huang RM, Gao WP, Zuo JM, Zhang XF, Misture ST, Chen Y, Lockard JV, Zhang BL, Guo SM, Khoshi MR, Dooley K, He HX, Wang Y (2015) An ion-exchange promoted phase transition in a Li-excess layered cathode material for high-performance lithium ion batteries. Adv Energy Mater 5(9):1401937
21. Ma DT, Zhang PX, Li YL, Ren XZ (2015) $Li_{1.2}Mn_{0.54}Ni_{0.13}Co_{0.13}O_2$-encapsulated carbon nanofiber network cathodes with improved stability and rate capability for Li-ion batteries. Sci Rep 5:11257
22. Wei GZ, Lu X, Ke FS, Huang L, Li JT, Wang ZX, Zhou ZY, Sun SG (2010) Crystal habit-tuned nanoplate material of $Li[Li_{1/3-2x/3}Ni_xMn_{2/3-x/3}]O_2$ for high-rate performance lithium-ion batteries. Adv Mater 22(39):4364–4367
23. Hosono E, Kudo T, Honma I, Matsuda H, Zhou HS (2009) Synthesis of single crystalline spinel $LiMn_2O_4$ nanowires for a lithium ion battery with high power density. Nano Lett 9(3):1045–1051. https://doi.org/10.1021/nl803394v
24. Zheng ZM, Cheng YL, Yan XB, Wang RT, Zhang P (2014) Enhanced electrochemical properties of graphene-wrapped $ZnMn_2O_4$ nanorods for lithium-ion batteries. J Mater Chem A 2(1):149–154. https://doi.org/10.1039/C3TA13511J
25. Zhang XL, Cheng FY, Yang JG, Chen J (2013) $LiNi_{0.5}Mn_{1.5}O_4$ porous nanorods as high-rate and long-life cathodes for Li-ion

batteries. Nano Lett 13(6):2822–2825. https://doi.org/10.1021/nl401072x

26. Chan CK, Peng HL, Liu G, McIlwrath K, Zhang XF, Huggins RA, Cui Y (2008) High-performance lithium battery anodes using silicon nanowires. Nat Nanotechnol 3(1):31–35. https://doi.org/10.1038/nnano.2007.411
27. Zhao JQ, Wang H, Xie ZQ, Ellis S, Kuai XX, Guo J, Zhu X, Wang Y, Gap LJ (2016) Tailorable electrochemical performance of spinel cathode materials via in-situ integrating a layered Li_2MnO_3 phase for lithium-ion batteries. J Power Sources 333:43–52. https://doi.org/10.1016/j.jpowsour.2016.09.145
28. Zhao JQ, Wang Y (2014) High-capacity full lithium-ion cells based on nanoarchitectured ternary manganese-nickel-cobalt carbonate and its lithiated derivative. J Mater Chem A 2(36):14947–14956. https://doi.org/10.1039/C4TA02574A
29. Armstrong AR, Holzapfel M, Novak P, Johnson CS, Kang SH, Thackeray MM, Bruce PG (2006) Demonstrating oxygen loss and associated structural reorganization in the lithium battery cathode $Li[Ni_{0.2}Li_{0.2}Mn_{0.6}]O_2$. J Am Chem Soc 128(26):8694–8698
30. Lu J, Zhan C, TP W, Wen JG, Lei Y, Kropf AJ, HM W, Miller DJ, Elam JW, Sun YK, Qiu XP, Amine K (2014) Effectively suppressing dissolution of manganese from spinel lithium manganate *via* a nanoscale surface-doping approach. Nat Commun 5:5693. https://doi.org/10.1038/ncomms6693
31. Wang HQ, Lai FY, Li Y, Zhang XH, Huang YG, SJ H, Li QY (2015) Excellent stability of spinel $LiMn_2O_4$-based cathode materials for lithium-ion batteries. Electrochim Acta 177:290–297. https://doi.org/10.1016/j.electacta.2015.02.027
32. Xie ZQ, Eikhuemelo H, Zhao JQ, Cain C, Xu WW, Wang Y (2015) Ni and Fe dual-doped $Li_4Mn_5O_{12}$ spinels as cathode materials for high-voltage Li-ion batteries. J Electrochem Soc 162(8):1523–1529
33. Xie ZQ, Ellis S, Xu WW, Dye D, Zhao JQ, Wang Y (2015) A novel preparation of core-shell electrode materials via evaporation-induced self-assembly of nanoparticles for advanced Li-ion batteries. Chem Commun 51(81):15000–15003. https://doi.org/10.1039/C5CC05577F
34. Shi SJ, JP T, Tang YY, Yu YX, Zhang YQ, Wang XL (2013) Synthesis and electrochemical performance of $Li_{1.13}1Mn_{0.504}Ni_{0.243}Co_{0.122}O_2$ cathode materials for lithium ion batteries via freeze drying. J Power Sources 221:300–307. https://doi.org/10.1016/j.jpowsour.2012.08.031
35. Shi SJ, Mai YJ, Tang YY, Gu CD, Wang XL, Tu JP (2012) Preparation and electrochemical performance of ball-like $LiMn_{0.4}Ni_{0.4}\ Co_{0.2}O_2$ cathode materials. Electrochim Acta 77:39–46. https://doi.org/10.1016/j.electacta.2012.05.110
36. Shi SJ, Tu JP, Zhang YD, Zhang YJ, Gu CD, Wang XL (2013) Morphology and electrochemical performance of li $[Li_{0.2}Mn_{0.56}Ni_{0.16}Co_{0.08}]O_2$ cathode materials prepared with different metal sources. Electrochim Acta 109:828–834. https://doi.org/10.1016/j.electacta.2013.08.002
37. Mohanty D, Kalnaus S, Meisner RA, Rhodes KJ, Li JL, Payzant EA, Wood DL, Daniel C (2013) Structural transformation of a lithium-rich $Li_{1.2}Co_{0.1}Mn_{0.55}Ni_{0.15}O_2$ cathode during high voltage cycling resolved by in situ X-ray diffraction. J Power Sources 229:239–248. https://doi.org/10.1016/j.jpowsour.2012.11.144
38. Hy S, Felix F, Rick J, Su WN, Hwang BJ (2014) Direct in situ observation of Li_2O evolution on Li-ich high-capacity cathode material, $Li[Ni_xLi_{(1-2x)/3}Mn_{(2-x)/3}]O_2$ $(0 \leq \times \leq 0.5)$. J Am Chem Soc 136(3):999–1007